8.4 THE BIRTH AND DEATH OF THE MJO: AN OBSERVATIONAL STUDY

James J. Benedict*
David A. Randall
Colorado State University, Fort Collins, Colorado

1. Introduction

The Madden-Julian Oscillation (MJO), an equatorial wave type first noted in the early 1970s (Madden and Julian, 1971, 1994), involves multiscale cloud and precipitation processes and is manifested in numerous atmospheric variables. Despite decades of research, the combination of a poor representation of this tropical wave in most current general circulation models (GCMs) and a lack of comprehensive understanding of several of its mechanisms highlights the need for continued exploration of the MJO. This report focuses on the "birth" (approaching wet phase) and "death" (departing wet phase) of the MJO and their related precipitation, convective, and advective processes using a host of observational datasets.

A number of studies have provided valuable insights into the structure and associated physical mechanisms of the MJO. In particular, the general characteristics and lifecycle of the wave as seen in a number of atmospheric variables have been researched [Hendon and Salby 1994 (HS94), DeMott and Rutledge 1998, Maloney and Hartmann 1998 (MH98), Meyers and Waliser 2003]. The convective and stratiform cloud and precipitation processes during the MJO wet phase have also been investigated [Lin and Johnson 1996a,b (LJ96a,b), Kikuchi and Takayabu 2004]. Several other studies have focused on the regional environment within which wave initiation occurs in the Indian Ocean and what related mechanisms are most important [Bladé and Hartmann 1993, Hu and Randall 1994, Kemball-Cook and Weare 2001 (K-CW01)]. Straub and Kiladis (2003; SK03) examined the structure of convectively-coupled Kelvin waves, a type of wave that closely resembles the MJO.

The purpose of this study is to explore certain features of the MJO—particularly the approach and departure of the wet phase—using analyses of both single events and event composites based on hydrological data from the Tropical Rainfall Measuring Mission (TRMM). We focus on the cloud and advective processes, as gathered from reanalysis datasets, that are associated with an evolving MJO event. We will also compare our composite results with proposed wave instability theories, including wave-CISK, wind-induced surface heat exchange (WISHE), stratiform instability, and the discharge-recharge mechanism. A novel aspect of this study is that it deals with the immediate and delayed drying processes following the MJO wet phase. This facet of the MJO lifecycle has not been analyzed explicitly in previous observational composite studies; rather, most studies (e.g., HS94; MH98) have implemented smoothed or filtered data fields to highlight the drying associated with Rossby wave circulations. In addition, the approach of basing MJO composite events on TRMM daily rainfall is unique among recent scientific endeavors.

Corresponding author address: James J. Benedict, Dept. of Atmospheric Science, Colorado State University, Fort Collins, CO 80523-1373.

Email: jim@atmos.colostate.edu

2. Data and Methodology

a. Data sources

The datasets used in the present study are drawn from three sources: TRMM, ERA40 (European Centre for Medium-Range Weather Forecasts 40-year reanalysis), and MODIS-Terra (Moderate Resolution Imaging Spectroradiometer–Terra satellite).

Our primary source for precipitation estimates is the TRMM satellite. The TRMM daily 1°x1° (1 Jan 1998–28 Feb 2004) data product 3B42-V5 is derived from a number of space-borne instruments (see Kummerow et al. 2000). TRMM's precipitation radar, the first radar instrument designed to operate onboard a satellite, provides unparalleled rainfall resolution and accuracy. This, combined with improved microwave and visible/infrared instrumentation as well as a sufficiently long data record (7+ years) offers the opportunity to study the MJO based on accurate, high-resolution rainfall data. Although our results based on dynamical fields are entirely independent of the TRMM data products, we are reassured by how well these dynamical fields match up with TRMM's hydrological patterns. We employ ERA40 data (daily, 2.5°x2.5°, 1 Jan 1997–31 May 2002) to describe the dynamic and thermodynamic state of the atmosphere during our period of analysis. A host of hydrological, radiational, and chemical parameters are found in the MODIS-Terra MOD08 D3 dataset (daily, 1°x1°, 2 March 2000–28 Feb 2004), but our analysis will utilize only cloud-top pressure (CTP) and temperature (CTT) data. A CO_2 slicing method centered on the 15-μm band is implemented in calculating CTP. While the accuracy of CTP in the context of multiple cloud layers is difficult to characterize, CTP values for non-overlapping clouds above 700 hPa are accurate to within 50 hPa (see Platnick et al. 2003 and King et al. 2003 for review).

b. Methodology

A number of statistical techniques are applied to the data. To isolate features that are related to the MJO, we spectrally analyze and filter several variables in zonal wavenumber and frequency space. Distinct convective episodes associated with the MJO are composited based on maximum daily TRMM rainfall.

Further statistical parameters, such as covariances, are derived from these composites.

Our spectral analysis of TRMM rainfall follows the procedure of Wheeler and Kiladis (1999, hereafter WK99). Although WK99 spectrally analyzed OLR in a wavenumber-frequency diagram (see Fig. 3 from their paper), our results based on TRMM precipitation are very similar (not shown). In addition to spectral analysis, we also implement spectral filtering methods to extract particular wave features from the raw data. Despite the high degree of spatial and temporal variability of equatorial rainfall, we find that the larger-scale rain structures, especially in a meridionally-averaged sense, are captured reasonably well by spectral filtering over the periods and wavenumbers of interest.

To filter the data, the mean and first three harmonics of the composite annual cycle are subtracted from the full data record. The first and last 10% of the timeseries are also tapered to mitigate spectral leakage. These anomalies are next transformed into zonal wavenumber-frequency space via complex fast Fourier transforms (FFTs). We isolate signals characterized by eastward-propagating waves of wavenumber 1-5 and period 20-100 days. Parallel analysis is also undertaken using a 10-100 day filter. For comparison, WK99 use wavenumbers 1-5 and periods 30-96 days, and K-CW01 effectively retain wavenumbers 1-6 and periods 10-100 days as spectral thresholds appropriate for MJO filtering. To obtain the MJO signal in physical space, all Fourier coefficients outside of the wavenumber-frequency thresholds are set to zero, and an inverse FFT is performed (opposite sequence to "forward" FFT). The resulting map timeseries represents that portion of the total signal associated with MJO-like variability in physical units. Versions of this MJO-filtered dataset are implemented in (a) distinguishing individual convective events associated with the MJO phenomenon and (b) the construction of a composite MJO event. We analyze the convective events in two frameworks; the first involves a timeseries of meridionally-averaged (10°S-5°N) rainfall anomalies, and the second involves a timeseries from an individual gridpoint.

In the meridionally-averaged framework, the MJO-filtered data is standardized based on an area-averaged mean and standard deviation (0°-360°, 10°S-10°N). This procedure serves to clarify rainfall events in the highly variable tropical Indian and West Pacific Oceans while tempering signals not associated with the MJO outside this region. Hovmöller diagrams (10°S-5°N) of the standardized data are then constructed. Individual convective events are defined according to a stringent set of criteria, similar in nature to the constraints imposed by Rui and Wang (1990). To qualify as an MJO convective episode, the standardized, filtered rainfall anomaly (R) in the Hovmöller diagram must exceed 1σ in strength and 20° in longitude throughout its lifetime, which must be a minimum of 15 days. During its lifetime, R must also exceed 1.5σ at some point. The entire event must occur in the Indian or West Pacific Ocean region (50°E-140°W) during the boreal non-summer months (15 September–31 May). The 17 MJO convective events defined under these constraints are visually verified by comparison with Hovmöller diagrams of raw, unfiltered TRMM rainfall.

A goal of this paper is the exploration of the atmospheric dynamics and cloud characteristics during the developmental and decaying stages of the MJO. Such processes of interest occur on spatial and temporal scales possibly eliminated during spectral filtering. In an attempt to return to these convective processes under the umbrella of the larger-scale MJO wave, we use the defined events based on R simply as a guide. For each event, the longitude and time of maximum R is recorded. This longitude and time become the centerpoint of a search area using an identical Hovmöller diagram (summed 10°S-5°N) of *raw, unfiltered* TRMM rainfall. We devised the search area, which scans ±15° longitude and ±5 days for the maximum meridionally-averaged rainfall value, because the date and location of the filtered precipitation maximum often was not collocated with its unfiltered counterpart. Following the search procedure, the resulting longitude and time of the unfiltered rainfall maximum defines the *base point* (lag day 0) of the event, upon which all other variables are centered (zonal wind, specific humidity, etc.). We analyze the timeseries of this base point, a meridional averaging at fixed longitude, from 30 days prior to rain maximum (lag -30) to 20 after rain maximum (lag +20). The rainfall maximum base point is implemented in the construction of time-height cross-sections of other variables for all defined MJO events, and these events are composited. The final composites of these variables are converted into anomaly forms, defined as departures from the mean atmospheric state during an MJO convective event (details provided in thesis, see web address in references). This anomaly definition guarantees a zero time mean for the event span, a useful feature for later statistical analyses.

In addition to the meridionally-averaged framework, we also define events based on a single gridpoint using a similar procedure. The point-based analysis is conducted to identify any highly localized features that may be masked by meridional averaging. Similar thresholds to those of the meridionally-averaged case are implemented to defined events, with the exception of slightly stronger σ constraints (to account for the absence of averaging) and the inclusion of a ±2° latitudinal search parameter.

c. Sensitivity testing of event selection criteria

Thorough testing on the sensitivity of all parameters involved in the event selection process was undertaken. The final composite results are not strongly sensitive to adjustments in the search area, but are weakly sensitive to the periods used in the initial step of filtering the raw data (20-100 days vs. 10-100 days). We discovered that the maximum MJO signal using the 20-100-day filter was on average 3-4 days later than and 7°-8° east of the maximum signal as detected by the 10-100-day filter. In essence, the same eastward-propagating convective envelopes associated with the MJO are detected, but they are detected at different times and locations in their

respective lifecycles. Despite this caveat, the coherent structure of the MJO convective envelope is assumed to remain nearly identical given a change of only a few days or a few degrees of longitude. Nonetheless, we must note that some differences do exist.

3. Results and Discussion

a. Results I: Basic variables

A comparison of TRMM and ERA40 total winter (Oct-Apr) precipitation is displayed in Figure 1. Although these datasets span slightly different temporal ranges, we assert that more than six years of

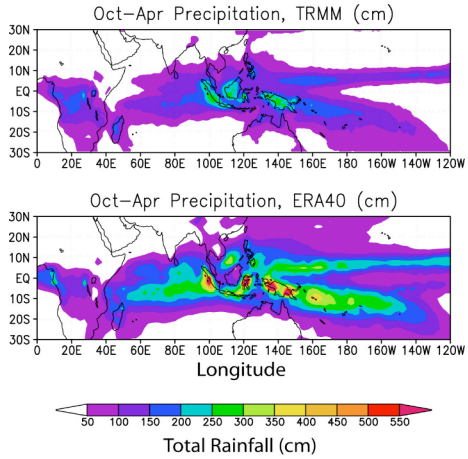

Figure 1. Total boreal winter rainfall from TRMM (top) and ERA40 (bottom).

data is sufficient to capture the general features of tropical rainfall. Examination of Fig. 1 suggests that the ERA40 dataset generally overestimates rainfall as seen from TRMM by 50-100 cm during boreal winter. Additional analyses (not shown) indicate that the precipitation from ERA40 also exhibits significantly higher temporal variance than that from TRMM. Despite these discrepancies, we feel strongly that many non-precipitation variables of the ERA40 dataset—including horizontal and vertical winds, temperature, moisture, pressure, and surface fluxes—are acceptable for use in an analysis of the MJO, especially in the context of meridional averaging and compositing.

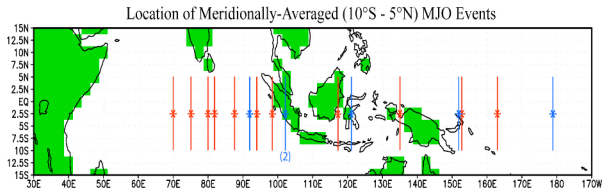

Figure 2. Map of MJO events (longitude of maximum rainfall), detected in both TRMM (red and blue) and ERA40 (red only) datasets, that make up the composite cross-sections for the meridionally-averaged (10°S-5°N) framework.

MJO events for the meridionally-averaged framework are displayed in Figure 2. Of the 17 MJO events detected by the TRMM satellite, 11 are contained in ERA40 and 13 in the MODIS dataset. The locations of peak convection occur across a range of geographic regions, from the central Indian Ocean to the International Date Line. For the gridpoint-based MJO events (map not shown), 13 are detected by TRMM, of which nine are contained in both ERA40 and MODIS datasets. None of the gridpoint events occur over land masses, and any events with unreasonable or unphysical data values are discarded.

The meridionally-averaged composite time-height cross-sections for selected variables are presented in Figures 3 and 4. Zonal wind cross-sections (not shown) indicate the expected transition from surface easterlies prior to intense rain to westerlies following maximum rain. The vertical velocity profile (not shown) suggests weak upward motion in the lower troposphere 5-15 days prior to deep convection.

The profile of specific humidity (q'; Fig. 3) indicates that prior to intense convection, abnormally dry air is observed during the suppressed phase of the MJO through much of the troposphere. Beginning around day -20, there is a tendency for weak, shallow moistening to develop below 900 hPa, possibly due to the collective effects of shallow convective clouds. Positive moisture anomalies rise from 900 hPa to higher than 500 hPa between days -15 and -10. This moistening coexists with weak $\omega' < 0$ and $T' > 0$, supporting the view that shallow cumuli play a role in preconditioning the atmosphere for later intense convection through destabilization (K-CW01, SK03). Low-level drying (800-925 hPa) begins on day 0 and expands vertically up to the 650 hPa level by day +7. After this time, most of the troposphere abruptly returns to an anomalously dry state.

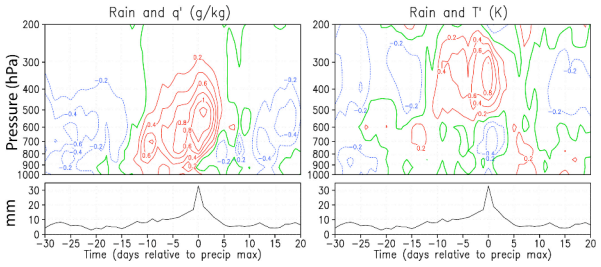

Figure 3. Time-height cross-sections of specific humidity (q'; l) and temperature (T'; r) for the meridionally-averaged framework (10°S-5°N). The corresponding composite TRMM rainfall timeseries is plotted below both panels. Solid red lines (dashed blue, solid green) are positive (negative, zero) departures from the MJO background state. Lag days relative to maximum rain appear on the horizontal axis.

Perturbations of meridionally-averaged temperature (T') are also presented in Fig. 3. At the time of maximum rainfall, much of the middle and upper troposphere is anomalously warm with a peak temperature perturbation of 0.9 K at 300-400 hPa. Simultaneously, cool anomalies occur below 550 hPa and near tropopause level. The structure of the low-level cooling closely matches previous results based on radiosonde data (SK03, LJ96a), and likely arises

from latent cooling of air within downdrafts (Reed and Recker, 1971) and stratiform precipitation processes (Houze, 1982).

The MODIS-derived CTP (Figure 4, left) and solar absorption at the surface (SSA'; Fig. 4, right, dashed purple line) suggest a distinct temporal asymmetry, with a gradual decrease in both variables prior to the wet phase followed by a rapid return to the background state afterward. SST' (Fig. 4, right, solid orange line) generally rises between days -30 and -11 during which time $SSA' > 0$, suggesting less cloud coverage, weak ocean surface mixing, and minimal rainfall. SST' decline as deeper convection develops, and are minimized during the westerly wind burst (WWB; LJ96a) 1-2 weeks following maximum rainfall.

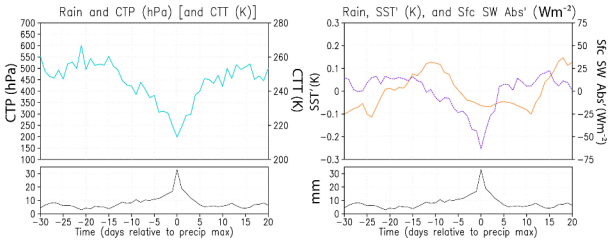

Figure 4. As in Fig. 3, but for MODIS cloud-top pressure (CTP; left vertical axis) and temperature (CTT; right vertical axis) (l), and sea-surface temperature (SST'; solid orange) and surface solar absorption (SSA'; dashed purple) (r).

Profiles of q' and anomalous surface latent heat flux ($SLHF'$) for the single gridpoint framework are displayed in Figure 5. Though noisier due to fewer events composited and less spatial averaging, the gridpoint case shares the same features as the meridionally-averaged framework (this is true for most variables), with a gradual rise in the moisture maximum prior to intense rainfall. As in Fig. 3, evidence of weak low-level drying exists almost immediately following the peak rainfall. The $SLHF'$ profile suggests that latent energy exchanges between the atmosphere and ocean are maximized *following* intense rainfall, which hints that the WISHE mechanism does not play a critical role in the events of this composite. A secondary peak in $SLHF'$ is seen during the time of the WWB.

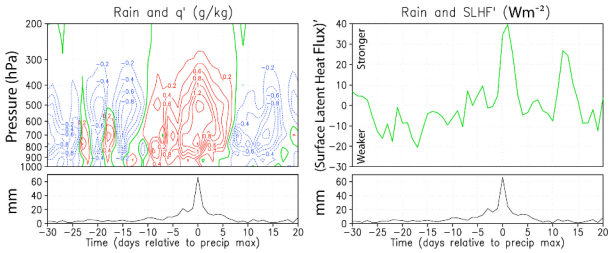

Figure 5. As in Fig. 3, but for q' (l) and surface latent heat flux ($SLHF'$, r) for the individual gridpoint framework. Corresponding TRMM rain composite for this framework appears below both panels.

b. Results II: Mechanisms of the MJO

Thus far, several important observations concerning the temporal and spatial evolution of the MJO have been presented. Key elements of an MJO wave passage include a gradual pre-convective heating and moistening of the lower troposphere occurring simultaneously with weak low-level upward motion, a transition to intense rainfall during the wet phase, and a rapid post-convective drying trend. In this section, we turn our attention to the advective and convective processes that relate to heat and moisture, as associated with the MJO. These mechanisms represent the effects of large-scale components and the *collective* effect of small-scale components, including intrusions of drier air from the subtropics and shallow cumulus transports. The term *collective* is used because small-scale processes such as heating by shallow cumulus growth occur on scales that are small compared to the area of the 2.5° x 2.5° (~8x10^2 km^2) ERA40 gridbox. While individual shallow cumuli have a small effect on the larger environment, over time the effect of the shallow cumulus *regime* can have a significant impact on the initiation and maintenance of the MJO (Nitta and Esbensen, 1974; LJ96b).

i. Horizontal and vertical components of advective transport of moisture

Our first investigation involving the advective processes associated with the MJO addresses specific humidity q. We conduct a moisture budget analysis by decomposing the anomalous time rate of change of q into horizontal and vertical components:

$$\frac{\partial q'}{\partial t} = -\left(u\frac{\partial q}{\partial x}\right)' - \left(v\frac{\partial q}{\partial y}\right)' - \left(\omega\frac{\partial q}{\partial p}\right)' + S'_q - C' \qquad (1)$$

Here, S'_q and C' are the sources and sinks of q. We chose the advective form of the moisture budget equation in order to diagnose changes in q at a particular point or latitudinal band. The contributions by the anomalous moisture sources and sinks (evaporation and condensation, respectively) are not explicitly analyzed due to the absence of these ERA40 data on individual pressure levels. Figure 6 depicts the combined effects of the horizontal and vertical components that contribute toward changes in q' for the meridionally-averaged case. Panel (a) displays the strong and immediate drying brought about by the horizontal wind component between day 0 and +5 (the "death" of the MJO). By comparison with panels (b) and (c), it is clear that the horizontal drying component has an impact on the moisture level, particularly during the first three days following the peak of the wet phase and at a pressure range of 650-850 hPa. This could perhaps be evidence of a lower-tropospheric dry jet punching eastward behind the intense convection, with the dry air originating in the subtropics. This topic will be addressed again with the aid of spatial maps in Section 3b*iv*. In essence, vertical advection is clearly important during the two weeks prior to intense rainfall, while post-convective drying is parsed into immediate (horizontal) and delayed (vertical; "subsidence") advective processes. The gridpoint-based results (not shown), a composite of fewer events, are less clear but indeed support the rapid horizontal and delayed

vertical drying in the lower troposphere. The concept of immediate and delayed drying mechanisms has not been explicitly discussed in previous studies. MH98

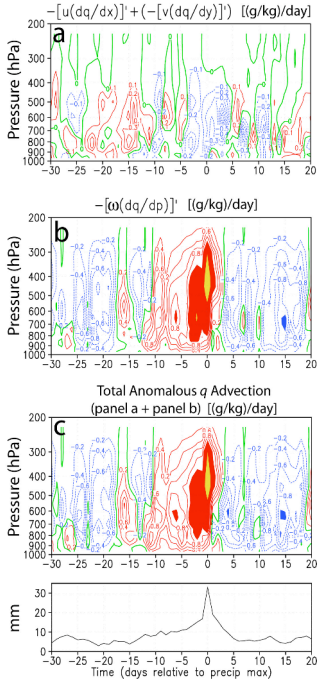

Figure 6. Time-height cross-sections of the (a) horizontal, (b) vertical, and (c) combined (horizontal + vertical) composites of the time rate of change of specific humidity for the meridionally-averaged framework. Contour type is identical to Fig. 3. Blue, red, and yellow shading indicate values less than -1.0 (g/kg)/day, between +1.0 and +2.0 (g/kg)/day, and greater than +2.0 (g/kg)/day, respectively.

investigate the rapid post-convective drying processes in the context of Rossby wave circulations emanating from the equatorial heat source (as in Gill, 1980). Our results support their findings, that drying is associated with strong lower-tropospheric westerly winds and boundary layer divergence at about two pentads following intense rainfall. We point out, however, that a more immediate drying component is seen in our reanalysis composites, a small-scale feature that might not be seen in the pentad-mean, bandpass-filtered data of MH98.

The importance of vertical advective moistening is highlighted in the single gridpoint cross-section (Figure 7; 10-100-day filtering). Between days

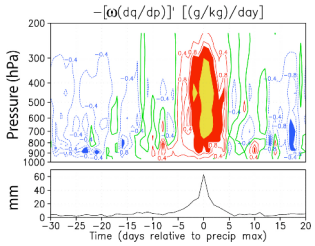

Figure 7. Time-height cross-section composite of the vertical component of the time rate of change of specific humidity for the individual gridpoint framework (derived with use of 10-100-day filter). Contour and shading schemes are identical to those in Fig. 6.

-5 and -15, episodic vertical q transport is noted. These "flame-like" features are generally capped at the 500 hPa level and are suggestive of the attempts of shallow cumuli and cumulus congestus in moistening and heating the lower troposphere.

ii. Convective processes of the MJO (Q_1 and Q_2)

We can infer that shallow convective processes are involved prior to intense rainfall by invoking the concepts of the apparent convective heat source (Q_1) and the apparent convective moisture sink (Q_2) (Yanai et al. 1973):

$$Q_1 \equiv Q_R + L(c-e) - \frac{\partial}{\partial p}\overline{s'\omega'}$$
$$= c_p\left[\frac{\partial T}{\partial t} + \mathbf{v}_h \cdot \nabla_h T + \left(\frac{p}{p_o}\right)^{\kappa} \omega \frac{\partial \theta}{\partial p}\right] \quad (2)$$

$$Q_2 \equiv L(c-e) + L\frac{\partial}{\partial p}\overline{q'\omega'}$$
$$= -L\left[\frac{\partial q}{\partial t} + \mathbf{v}_h \cdot \nabla_h q + \omega \frac{\partial q}{\partial p}\right] \quad (3)$$

In (2), Q_1 is a combined measure of heating by radiation (Q_R), net latent heating [$L(c-e)$], and the vertical convergence of sensible eddy heat transports. In (3), Q_2 represents the net latent heating and the vertical convergence of eddy moisture transports. The magnitude of atmospheric heating or cooling brought about by convective processes can be deduced by measuring perturbations in the heat and moisture

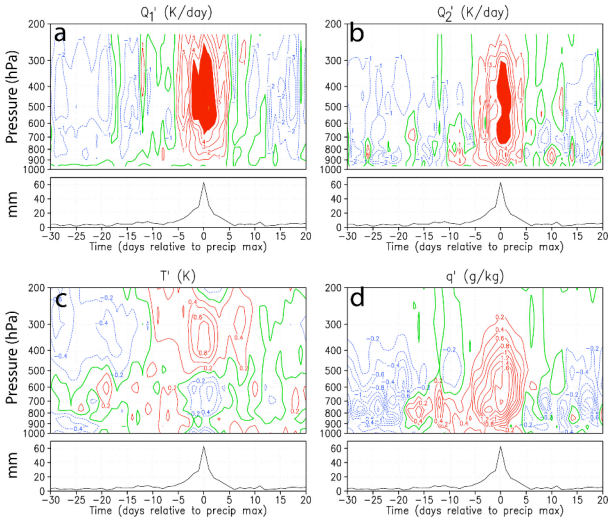

Figure 8. Time-height cross-section composites of (a) apparent heat source (Q_1'), (b) apparent moisture sink (Q_2'), (c) T', and (d) q' for the individual gridpoint framework (derived with use of 10-100-day filter). Contour type identical to Fig. 3. Red shading indicates values greater than 5 K/day.

budgets applied on large (ERA40 gridbox-sized) scales. If there are nonzero residuals computed from

the large-scale budget analyses [RHSs of (2) and (3)], these residuals represent the effects of "subgrid-scale" convection on the larger gridbox area.

Time-height cross-sections of Q_1' and Q_2' (Figure 8) for the 10-100-day filter single gridpoint framework point to tropospheric cooling prior to day –15, likely the result of radiational effects (see Eq. 2). Simultaneously, the Q_2' plot suggests low-level moistening due to surface evaporation. The key feature of Fig. 8 occurs between days -15 and -5 (MJO "birth"); at this time, positive temperature, moisture, and convective heating (Q_1') anomalies exist. Additionally, Q_2' shifts from moistening to drying, signifying a transition from lightly- or non-precipitating shallow clouds to deeper precipitating clouds. These observations combined indicate the presence and importance of growing shallow cumuli and their associated detrainment of moisture into the overlying dry mid-troposphere.

iii. Driving heat and moisture variances

Wave generation, amplification, and maintenance require an energy source. In the low latitudes, the generation of eddy available potential energy (EAPE) and its conversion to eddy kinetic energy (EKE) due to *localized* heating and moistening feed tropical waves. EAPE is associated with increases in T variance and is increased when $Q_1'T' > 0$. Vertical time-averaged profiles of $Q_1'T'$ and $-Q_2'q'$ for three stages leading up to deep convection are displayed in Figure 9.

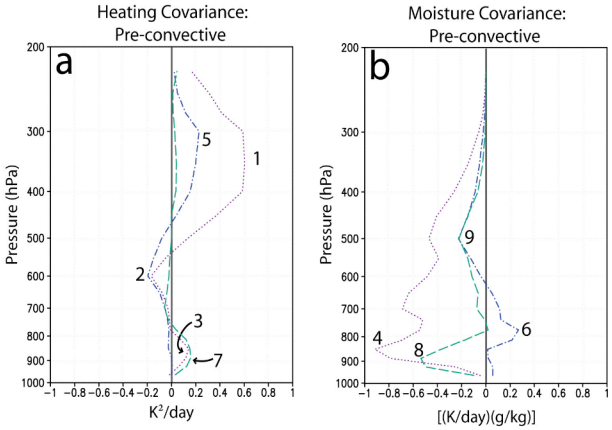

Figure 9. Vertical profiles of heating ($Q_1'T'$; l) and moistening ($-Q_2'q'$; r) averaged over three pre-convective stages for the individual gridpoint framework (derived with use of 10-100-day filter). Profiles are represented by dotted purple (days -30 to -15), dash-dot blue (days -15 to -10), and dashed aqua (days -10 to -5) lines. Numbers indicate features that may be discussed in the text.

Between days -15 and -10, an enhancement in the effectiveness of lower-tropospheric moistening by shallow cumuli, likely due to an increase in their number and coverage as evidenced by the decline in $SSA^{\dagger}$, heralds the end of the suppressed (dry) phase. The more widespread coverage of shallow cumuli is reflected in the profiles of ω', T', and q' (see Fig. 8). The heating and moistening covariance profiles (dot-dashed blue lines in Fig. 9) suggest that radiative cooling ("5" in Fig. 9) occurs above 450 hPa. Weak radiational cooling ("2") from the top of the mid-level warm (and progressively more moist) layer (see Fig. 8) also persists. Between 650 hPa and 800 hPa, detrainment from shallow cumuli has moistened and continues to moisten the layer. This observation, combined with only a minimal increase in precipitation, aids in increasing q variance at low levels ("6" in Fig. 9). Collectively, mid- and upper-level radiational cooling, elevated SSTs, and low-level heating and moistening effectively increase convective available potential energy (CAPE), thus destabilizing the atmosphere and preconditioning the region for an impending intensification of convection (e.g., K-CW01). These features lend support to the discharge-recharge theory rather then stratiform instability.

Increasing coverage, intensity, and vertical growth of cumuli occur between days -10 and -5. Upward vertical motions (not shown) and positive temperature and moisture perturbations (Fig. 8) become elevated and rapidly extend toward the upper troposphere as deep convection becomes more active. After a brief lull in rainfall, precipitation rates trend upward and are associated with a warming and drying at low levels. At this time, easterly wind anomalies become slightly stronger with upper-level westerly anomalies becoming more prominent (not shown). Several interesting features are noted in the day -10 to -5 covariance profiles (dashed aqua lines in Fig. 9). Although there is little activity above 400 hPa, low-level convective heating of warm, moist air ("7", $\overline{Q_1'T'} > 0$) below 775 hPa drives T variance and helps in the intensification of convective clouds. Simultaneously, the enhanced condensation rate (i.e., rainfall production) by growing cumuli dries the atmosphere below 800 hPa ("8" in Fig. 9), while these same clouds continue to detrain vapor into the overlying dry layer near 500 hPa (see Fig. 9), preparing the atmosphere for deep convection as in the discharge-recharge theory.

iv. Single event, gridpoint framework (21 October 1998)

The composite cross-sections presented thus far provide detailed information about the temporal and vertical variability of an MJO wave passage. To gain a flavor of the *horizontal* spatial characteristics of the tropical disturbance, we present map sequences (Figure 10) of rainfall, 850 hPa $\mathbf{v}'$, and 775 hPa q' and $\mathbf{v}'$ for a single MJO event centered at (2.5°S, 67.5°E) (the "origin point"; circled in each frame of Fig. 10) with corresponding total rainfall maximum of 80.1 mm on 21 October 1998 ("day 0"). This event shares many of the characteristics described in the composite map sequence (not shown), but is unique in that it appears to capture the initiation of an MJO event in the equatorial west-central Indian Ocean.

The development of intense rainfall at the origin point appears to be associated with a

strengthening of the Somali Jet and a slow migration of an anticyclonic gyre ("A" in Fig. 10) from southern India to its location just west of the origin point on day 0. During its migration, the northerly flow on the east side of the anticyclonic gyre encounters an increasingly stronger southeasterly flow near the origin point, greatly enhancing low-level convergence. An area of precipitation rapidly blossoms directly over the origin point on day -3 (not shown) and strengthens to its maximum intensity on day 0 (Fig. 10). For this event, intense rainfall developed *in situ* and did not propagate toward the origin point from the west, making this something of a unique situation. Also at this time, a dry air mass is seen over southern India and the Arabian Sea.

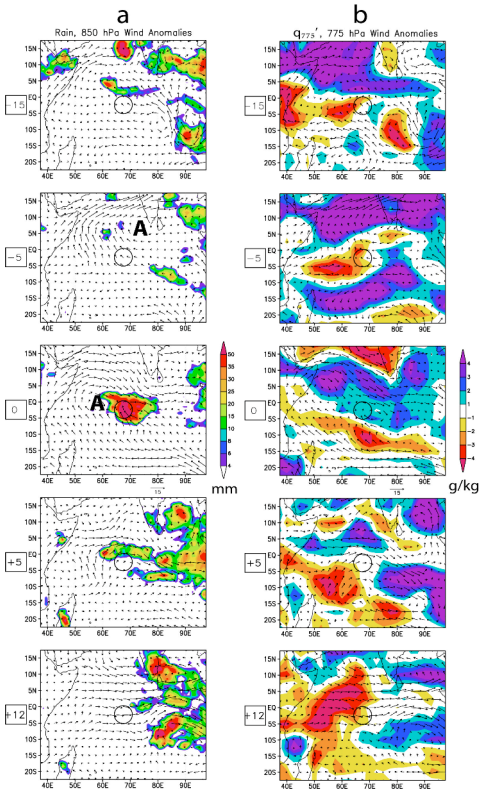

Figure 10. Map sequences of (a) TRMM total rain and $\mathbf{v}'_{850}$, and (b) q'_{775} and $\mathbf{v}'_{775}$ for the event of 21 October 1998 based on the individual gridpoint framework. Anomaly values represent departures from a climatological mean (1984-2001). Lag days are to the left of each panel. Maximum wind vector and shading scale are below and to the right of the zero lag day panel, respectively. The zero lag day corresponds to the day of maximum total rain at the geographical base point (2.5°S, 67.5°E, circled in each panel). Letters "A" and "C" represent anticyclonic and cyclonic gyres as discussed in the text.

After day 0, maximum precipitation shifts eastward to near 100°E by day +5. Concerning moisture, inspection of the q'_{775} (Fig. 10) and ω'_{775} (not shown) fields between days 0 and +5 indicates that a rapid drying trend at 775 hPa is associated with westerly $\mathbf{v}'$ but not sinking motion, further supporting the importance of the initial low-level advection of dry air by horizontal westerly wind anomalies as discussed in Section 3b*ii*. Another important feature noted in the low-level moisture field is the merging of dry air masses to the west of the origin point. The pocket of dry air at 775 hPa seen on day +5 (Fig. 10, day +5) drifts southward (not shown), eventually merging with an expanding dry air mass centered near (7.5°S, 50°E). Following the air mass merger, this very dry air and attendant subsidence are advected toward the origin point on day +12. Daily maps of anomalous precipitable water (not shown) clearly display the merging of independent, dry air masses of subtropical origin at approximately 10° west of the origin point. Following the merging of the air masses, lower-tropospheric dry air is advected to the origin point 2-4 days later. The dry air mass is associated with large and positive OLR', $PW' < 0$, $q' < 0$ at and below 600 hPa, and $\omega' > 0$ (sinking) below 600 hPa.

iv. Wave theories and the MJO: How does it work?

Over the past three decades, several theories have been proposed detailing the physical mechanisms that generate instability and wave amplification. Versions of these theories fall into four basic categories: wave-CISK, surface evaporation feedback (WISHE), stratiform instability, and discharge-recharge. In this section, we make use of the results of our analyses to determine the consistencies and differences between each proposed theory and the observations.

Wave-CISK involves instability that occurs as a result of "cooperation" between localized convective heating and its environmental large-scale circulation [e.g., Hayashi 1970, Lindzen 1974]. Possible evidence of wave-CISK-like processes is noted in the observation that initial robust convection [see Fig. 8; also, vertical separation of Q_1 and Q_2 peaks indicates vigorous convection (e.g., Johnson and Young 1983 or Luo and Yanai 1984)] appears to occur at and just prior to maximum low-level convergence as assessed by the temporal gradient of u' (not shown). Whether this convergence is a direct result of convective heating is unclear. Data of higher spatial resolution would be needed to confirm the precise relationships between convection and larger-scale low-level convergence. Below 500 hPa near day 0, a second-mode baroclinic structure (warm-over-cold) is associated with convective heating of anomalously-cool air (Fig. 8). This is inconsistent with wave-CISK-like theories which require a positive correlation between deep-layer warm anomalies and convective heating. From Fig. 8, deep convective heating lags low-level T' maxima by about 1-2 weeks (out of phase by more than 0.25 cycles as in SK03). It is possible that the inferred shallow cumuli partake in a CISK-like process in which shallow heating generates weak low-level moisture convergence, but this is beyond any application of the reanalysis data (2.5°x2.5°) being used in this study. Many inconsistencies between wave-CISK theory and observations, including phase speed and vertical structure differences and global circumnavigation aspects, are apparent. Overall,

certain elements may be important in the evolution of the MJO, but a direct application of the pure wave-CISK theory does not fully explain the observed oscillation.

The WISHE mechanism (e.g., Emanuel 1987) involves an instability that arises through the interaction of surface heat and moisture fluxes and large-scale wave dynamics. This theory states that eastward-propagating convective systems are maintained by increased inflow of low-level moisture, a result of surface evaporation from the ocean by anomalous easterlies. The results of this study—including the time-height composite cross-sections, spatial composites (not shown), and the single spatial event (Fig. 10)—suggest that the WISHE mechanism is not operating in the events examined. In general, surface fluxes and horizontal wind anomalies are stronger to the west of the disturbance. Even in the single spatial event, which occurred in the western Indian Ocean, surface fluxes (not shown) were very weak just prior to intense convection. Additionally, many events occurred in a region of climatological westerlies. Nonetheless, the contribution of ocean-atmosphere surface fluxes in the context of the MJO is not negligible.

Stratiform instability is generated by a positive correlation between a second-mode temperature profile and second-mode stratiform heating structure (Houze 1997, Mapes 2000). The theory of stratiform instability involves the interplay of convective and stratiform heating modes, such that reductions in convective inhibition (CIN) outweigh fluctuations in CAPE in the presence of a warm-over-cold temperature structure (Mapes, 2000). The resulting deep convection and attendant convective heating profile evolve into warm-over-cold stratiform heating, in positive correlation with the original T' structure (thus generating EAPE). Our results do not directly support pure stratiform instability theory for a few reasons. Instead of warm-over-cold anomalies leading intense convection, the MJO wave involves low-level warming and moistening underlying cool, dry anomalies, suggestive of an increase in CAPE rather than a decrease in CIN. Additionally, Mapes (2000) found that pure stratiform instability disturbances are associated with upper-tropospheric warm anomalies positioned about 30° east of maximum convection. Our observations indicate that upper-tropospheric warm anomalies are collocated with convective heating (Q_1'; Fig. 8). It is possible that the stratiform instability mechanism may be important between days 0 and +5 when stratiform processes appear to be most active (see Fig. 8c). Perhaps this mechanism prolongs convection and possibly the MJO wet phase itself by reducing CIN and regenerating or maintaining residual convection (e.g., see deep-layer $Q_1' > 0$ for days 0 to +5 in Fig. 8a).

The essence of discharge-recharge theory is that a local, gradual build-up of instability through low-level warming and moistening preconditions the atmosphere for episodes of deep convection associated with MJO-like waves. Several aspects of this gradual enhancement of instability and cumulus growth—as outlined in such papers as Bladé and Hartmann (1993), Hu and Randall (1994), and K-CW01—are noted in the results of this study. For example, time-height cross-sections of ω' (not shown), T', q' (Fig. 8), as well as profiles of CTP (Fig. 4), PW', SSA', and OLR' (not shown) clearly suggest a slow build-up of low-level warming, moistening, and cumulus growth.

Relative to the maximum total rainfall, our results indicate an asymmetry in timescales of the recharge and discharge phases such that convective dissipation and tropospheric drying occur more rapidly than cumulus growth and tropospheric moistening. In Figure 11, we present a schematic diagram of the discharge-recharge mechanism as seen in the reanalysis data. In terms of T' and q' (e.g., Figs. 8c and 8d), for instance, low-level warming and moistening are maximized for ~10-15 days, deep convection and precipitation processes ultimately serving to stabilize the troposphere are active for ~10 days, and suppressed convection with associated tropospheric drying are observed for ~15 days, thus yielding a 35-40-day oscillation. The timescale of these MJO stages might involve linkages between the hydrologic cycle and the ocean (Stephens et al., 2004) in addition to the atmospheric component as in Bladé and Hartmann (1993).

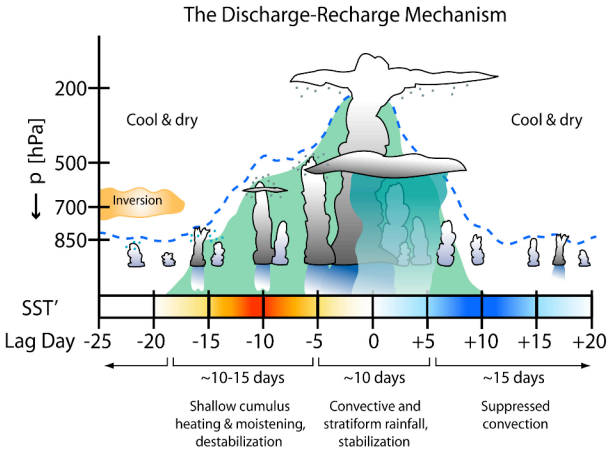

Figure 11. Time-height schematic diagram of the discharge-recharge mechanism. SST' (red = warmer, blue = cooler) and lag day relative to maximum rain appear along the horizontal axis. Stages of the discharge-recharge process, as seen in ERA40 data, appear below the horizontal axis. The approximate top level of convective cloud processes is indicated by the dashed blue line, while green shading represents the approximate area of $q' > 0$. Light blue dots above shallower convective clouds represent moistening via detrainment, while gray dots below stratiform clouds represent ice crystal fall-out and moistening. Convective precipitation is indicated by darker-blue rain shafts, and stratiform rain areas are light-blue and slightly transparent.

Evidence in support of the *localized* destabilization via low-level warming and moistening is noted in the fairly weak horizontal wind convergence (not shown) and dominance of anomalous vertical moisture transport (Fig. 6) over horizontal moisture transport ~5-15 days prior to maximum rainfall. Such observations suggest that, for most of the events in the composites presented, the build-up of low-level

heat and moisture is accomplished by *localized* mechanisms rather than by large-scale advective processes.

A final aspect of discharge-recharge theory worthy of comment concerns the spatial characteristics of the MJO events analyzed and their related triggering mechanisms. In this study, most of the individual events are located in the eastern Indian and western Pacific Ocean areas (Fig. 2). We chose these locations to correspond to maximum wet phase amplitude and not wave initiation, and so it is likely that the composite results largely reflect the evolution of a (nearly) fully-developed oscillation. Inspection of dry static stability ($\hat{\theta}' = \frac{\theta'_{250} - \theta'_{775}}{2}$; Fig. 12,l) supports this hypothesis, showing the shape of the $\hat{\theta}'$ profile to be quite similar to a model-generated stability composite of events 90° downstream of wave initiation (Fig. 11c in Bladé and Hartmann 1993). The individual event (21 October 1998) presented as spatial map sequences in Fig. 10 is also located in the western Indian Ocean and provides some support for discharge-recharge theory as interpreted by Bladé and Hartmann (1993; see their Fig. 11a). Although the signal is noisy, the $\hat{\theta}$ (Figure 12,r) indicates a steady decline in stability beginning near lag day -14 to -10, a minimum a few days prior to deep convection, and a rapid increase during the deep convection. Note the distinct differences between the left and right panels of Fig. 12. The destabilization near day -5 is likely due to

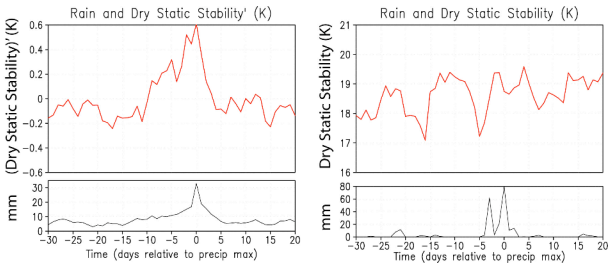

Figure 12. Composite timeseries of anomalous dry static stability for meridionally-averaged framework (l; see text for definition), and timeseries of dry static stability for the single event of 21 October 1998 based on the individual gridpoint framework (r). Corresponding TRMM rainfall profiles appear below both panels. Anomaly values for the left panel represent departures from climatology (1984-2001).

a sharp increase in moist static energy at 1000 hPa (h_{1000}), while h_{400} remains quite low (not shown). Additionally, the 21 October 1998 event appears to have ties to a subtropical trigger, albeit in the form of low-level convergence near the edge of an anticyclone rather than an area of upper-level divergence impinging on the Tropics as in Bladé and Hartmann (1993). Overall, the theory of localized destabilization and discharge-recharge mechanisms is highly appropriate in explaining many of the observed features of MJO wave evolution.

v. Comments on Statistical Significance

To assess the quantitative robustness of the major features being presented in this report, we compute statistical significance values. Fig. 8 indicates a very weak signal but of correct physical sign associated with general pre-convective heating and moistening of the lower levels. Areas of statistical significance, however, are not present where shallow cumulus activity is anticipated. In the first five days following intense rainfall, there is evidence of rapid drying associated with the increase in horizontal winds (Fig. 6). Significance plots (not shown) suggest that this drying may be statistically significant above the 90% level. There are many difficulties in applying the concepts of statistical significance to the results in this paper, mainly due to the relatively short TRMM data record. Despite these limitations, we should not completely discount the physical results. For example, although significance is below 90% in the lower troposphere between days -10 and -5 in a plot of Q'_1, active vertical moisture transport and warm, moist anomalies (see Figs. 7 and 8) suggest a physical link explained by shallow convective processes (shallow cumuli). Additionally, observational experiments such as TOGA COARE testify to the presence and importance of such shallow cloud activity. Concerning post-convective drying, strong, statistically significant westerly winds occur within five days after intense rainfall and occur simultaneously with a sharp low-level decrease in q'. Although only weak statistical significance is noted (not shown), the conclusion of rapid drying associated with increased zonal winds is not physically unreasonable and has been largely overlooked in previous research studies. We intend to further investigate these mechanisms in the future.

4. Concluding Remarks

This thesis focuses on a number of key elements involved in the "birth" and "death" of the MJO. The results of this report suggest that reanalysis data is of suitable use in capturing the mesoscale features of the approach and departure of the MJO wet phase. Most previous research studies utilize smoothed or filtered data fields that might miss potentially important small-scale features such as the immediate post-convective drying signal seen in the present study. We have also seen abundant evidence of shallow cumulus activity prior to intense MJO-related rainfall, a physical process that could be masked by smoothing or filtering. In general, the statistical approach used in analyzing certain MJO mechanisms must cater to the scale of that mechanism, which is why we elected to use unfiltered, high-resolution rainfall within a filtered, MJO-related convective envelope.

Our analysis highlights the importance of shallow convective heating and moistening by cumuli prior to the arrival of the intense rainfall (the "birth" of the MJO). During the two weeks leading up to day 0, convective vertical transport of T and q in the lower troposphere and extending into the middle troposphere plays a critical role in "preconditioning" the environment for deep convection, as in Bladé and Hartmann (1993) and K-CW01. Near day 0, precipitation processes evolve from convective to stratiform, according to the

vertical structures of Q_1 and Q_2. Concerning the "death" of the MJO, we note distinct vertical and temporal drying processes. The composite results indicate that there is a tendency for the horizontal winds ($\mathbf{v}_h$) to be associated with low-level drying soon after the most intense precipitation has ended. This drying related to the initial $\mathbf{v}_h$ maximum occurs a few days earlier than the onset of deep-layer subsidence and 1-2 weeks earlier than the most intense subsidence. Previous studies, including HS94 and MH98, implement smoothed data fields to analyze this delayed post-convective drying. While our results strongly support their findings, we point out that a more immediate drying associated with the horizontal winds may play an important role only a few days following intense rainfall.

In terms of wave theories in explaining instabilities and growth associated with the MJO, we find that many of our results are in support of the discharge-recharge hypothesis [Bladé and Hartmann (1993), Hu and Randall (1994), K-CW01]. Preconditioning of the atmosphere by low-level heating and moistening, a fundamental aspect of the discharge-recharge theory, is clearly noted in the results of this study. Although certain elements of generalized wave-CISK, WISHE, and stratiform instability mechanisms are seen, several inconsistencies prohibited a direct application of any one of these proposals to the observed MJO.

Although research on the MJO is currently entering its fourth decade, many aspects of this tropical wave remain a mystery. It is our intent to further explore the issues surrounding the MJO—including wave triggering mechanisms, extratropical connections, scale interactions, and cloud processes—in the near future. We also hope to incorporate simplified model and/or general circulation model tests as a means of examining the physical interactions that make the Madden-Julian Oscillation so complex.

REFERENCES

A full text report detailing many of the aspects that could not be included in this paper can be found at *http://kiwi.atmos.colostate.edu:16080/BUGS/groupPIX/jim/Pjim.html.* This paper was written as part of the Masters thesis project of the first author.

Bladé, I., and D. L. Hartmann, 1993: Tropical Intraseasonal Oscillations in a Simple Nonlinear Model. *J. Atmos. Sci.*, **50**, 2922-2939.

DeMott, C. A., and S. A. Rutledge, 1998: The Vertical Structure of TOGA COARE Convection. Part II: Modulating Influences and Implications for Diabatic Heating. *J. Atmos. Sci.*, **55**, 2748-2762.

Emanuel, K. A., 1987: An Air-Sea Interaction Model of Intraseasonal Oscillations in the Tropics. *J. Atmos. Sci.*, **44**, 2324-2340.

Gill, A. E., 1980: Some Simple Solutions for Heat Induced Tropical Circulation. *Quart. J. Roy. Meteor. Soc.*, **106**, 447-462.

Hayashi, Y., 1970: A Theory of Large-Scale Equatorial Waves Generated by Condensation Heat and Accelerating the Zonal Wind. *J. Meteor. Soc. Japan*, **48**, 140-160.

Hendon, H. H., and M. L. Salby, 1994: The Life Cycle of the Madden-Julian Oscillation. *J. Atmos. Sci.*, **51**, 2225-2237.

Houze, R. A., Jr., 1982: Cloud Clusters and Large-Scale Vertical Motions in the Tropics. *J. Meteor. Soc. Japan*, **60**, 396-410.

———, 1997: Stratiform Precipitation in Regions of Convection: A Meteorological Paradox? *Bull. Amer. Meteor. Soc.*, **78**, 2179, 2196.

Hu, Q., and D. A. Randall, 1994: Low-Frequency Oscillations in Radiative-Convective Systems. *J. Atmos. Sci.*, **51**, 1089-1099.

Johnson, R. H., and G. Young, 1983: Heat and Moisture Budgets of Tropical Mesoscale Anvil Clouds. *J. Atmos. Sci.*, **40**, 2138-2147.

Kemball-Cook, S. R., and B. C. Weare, 2001: The Onset of Convection in the Madden-Julian Oscillation. *J. Climate*, **14**, 780-793.

Kikuchi, K., and Y. N. Takayabu, 2004: The Development of Organized Convection Associated with the MJO during TOGA COARE IOP: Trimodal Characteristics. *Geophys. Res. Lett.*, **31**, L10101.

King, M. D., W. P. Menzel, Y. J. Kaufman, D. Tanré, B.-C. Gao, S. Platnick, S. A. Ackerman, L. A. Remer, R. Pincus, and P. A. Hubanks, 2003: Cloud and Aerosol Properties, Precipitable Water, and Profiles of Temperature and Water Vapor from MODIS. *IEEE Transactions on Geoscience and Remote Sensing*, **41**, 442-458.

Kummerow, C., J. Simpson, O. Thiele, W. Barnes, A. T. C. Chang, E. Stocker, R. F. Adler, A. Hou, R. Kakar, F. Wentz, P. Ashcroft, T. Kozu, Y. Hong, K. Okamoto, T. Iguchi, H. Kuroiwa, E. Im, Z. Haddad, G. Huffman, B. Ferrier, W. S. Olson, E. Zipser, E. A. Smith, T. T. Wilheit, G. North, T. Krishnamurti, and K. Nakamura, 2000: The Status of the Tropical Rainfall Measuring Mission (TRMM) After Two Years in Orbit. *J. Appl. Meteor.*, **39**, 1965-1982.

Lin, X., and R. H. Johnson, 1996a: Kinematic and Thermodynamic Characteristics of the Flow Over the Western Pacific Warm Pool during TOGA COARE. *J. Atmos. Sci.*, **53**, 695-715.

———, and ———, 1996b: Heating, Moistening, and

Rainfall over the Western Pacific Warm Pool during TOGA COARE. J. Atmos. Sci., **53**, 3367-3383.

Lindzen, R. S., 1974: Wave-CISK in the Tropics. *J. Atmos. Sci.*, **31**, 156-179.

Luo, H., and M. Yanai, 1984: The Large-Scale Circulation and Heat Sources over the Tibetan Plateau and Surrounding Areas during the Early Summer of 1979. Part II: Heat and Moisture Budgets. *Mon. Wea. Rev.*, **112**, 966-989.

Madden, R. A., and P. R. Julian, 1971: Description of a 40-50 Day Oscillation in the Zonal Wind in the Tropical Pacific. *J. Atmos. Sci.*, **28**, 702-708.

———, and ———, 1994: Observations of the 40-50-Day Tropical Oscillation — A Review. *Mon. Wea. Rev.*, **123**, 814-837.

Maloney, E. D., and D. L. Hartmann, 1998: Frictional Moisture Convergence in a Composite Life Cycle of the Madden-Julian Oscillation. *J. Climate*, **11**, 2387-2403.

Mapes, B. E., 2000: Convective Inhibition, Subgrid-Scale Triggering Energy, and Stratiform Instability in a Toy Tropical Wave Model. *J. Atmos. Sci.*, **57**, 1515-1535.

Meyers, D. S., and D. E. Waliser, 2003: Three-Dimensional Water Vapor and Cloud Variations Associated with the Madden-Julian Oscillation during Northern Hemisphere Winter. *J. Climate*, **16**, 929-950.

Nitta, T., and S. Esbensen, 1974: Heat and Moisture Budget Analyses Using BOMEX Data. *Mon. Wea. Rev.*, **102**, 17-28.

Platnick, S., M. D. King, S. A. Ackerman, W. P. Menzel, B. A. Baum, J. C. Riédi, and R. A. Frey, 2003: The MODIS Cloud Products: Algorithms and Examples from Terra. *IEEE Transactions on Geoscience and Remote Sensing*, **41**, 459-473.

Reed, R. J., and E. E. Recker, 1971: Structure and Properties of Synoptic-Scale Wave Disturbances in the Equatorial Western Pacific. *J. Atmos. Sci.*, **28**, 1117-1133.

Rui, H., and B. Wang, 1990: Development Characteristics and Dynamic Structure of Tropical Intraseasonal Convection Anomalies. *J. Atmos. Sci.*, **47**, 357-379.

Stephens, G. L., P. J. Webster, R. H. Johnson, R. Engelen, and T. L'Ecuyer, 2004: Observational Evidence for the Mutual Regulation of the Tropical Hydrological Cycle and Tropical Sea Surface Temperatures. *J. Climate*, **17**, 2213-2224.

Straub, K. H., and G. N. Kiladis, 2003: The Observed Structure of Convectively Coupled Kelvin Waves: Comparison with Simple Models of Coupled Instability. *J. Atmos. Sci.*, **60**, 1655-1668.

Wheeler, M., and G. N. Kiladis, 1999: Convectively Coupled Equatorial Waves: Analysis of Clouds and Temperature in the Wavenumber-Frequency Domain. *J. Atmos. Sci.*, **56**, 374-399.

Yanai, M., S. Esbensen, and J.-H. Chu, 1973: Determination of Bulk Properties of Tropical Cloud Clusters from Large-Scale Heat and Moisture Budgets. *J. Atmos. Sci.*, **30**, 611-627.